IOP Publishing Phys. Med. Biol. 63 (2018) 055011(9pp) https://doi.org/10.1088/1361-6560/aa9e32

Physics in Medicine & Biology

IPEM Institute of Physics and Engineering in Medicine

PAPER

Fixed forced detection for fast SPECT Monte-Carlo simulation

T Cajgfinger, S Rit, J M Létang, A Halty and D Sarrut

Université de Lyon, CREATIS, CNRS UMR5220; Inserm U1044, INSA-Lyon, Université Lyon 1, Centre Léon Bérard, France

E-mail: david.sarrut@creatis.insa-lyon.fr

RECEIVED
12 May 2017

REVISED
24 November 2017

ACCEPTED FOR PUBLICATION
29 November 2017

PUBLISHED
2 March 2018

Keywords: Monte-Carlo simulations, SPECT, variance reduction

Abstract

Monte-Carlo simulations of SPECT images are notoriously slow to converge due to the large ratio between the number of photons emitted and detected in the collimator. This work proposes a method to accelerate the simulations based on fixed forced detection (FFD) combined with an analytical response of the detector. FFD is based on a Monte-Carlo simulation but forces the detection of a photon in each detector pixel weighted by the probability of emission (or scattering) and transmission to this pixel. The method was evaluated with numerical phantoms and on patient images. We obtained differences with analog Monte Carlo lower than the statistical uncertainty. The overall computing time gain can reach up to five orders of magnitude. Source code and examples are available in the Gate V8.0 release.

1. Introduction

Monte-Carlo simulations of SPECT images are useful for various applications such as designing imaging systems, investigating quantitative imaging or in targeted radionuclide therapy. However, they are notoriously slow to converge due in particular to the large ratio between the number of photons emitted, denoted 'primaries' in the following, and detected in the SPECT head (collimator + detector). Due to the solid angle of the detector and the loss of photons in the collimator, only one emitted photon in about 10^4 reaches the detector plane. This makes SPECT Monte-Carlo simulation a slow process, as every photon must be tracked and can generate secondary photons that should also be tracked through the detector. With 'brute-force' Monte-Carlo methods, this can lead to very long simulation times, up to a few days for the simulation of a complete Siemens Symbia *T* system (Descourt *et al* 2010).

In order to decrease the computation time, several variance reduction techniques (VRT) have been developed (Haynor *et al* 1991). The geometrical importance sampling (De Beenhouwer 2009) approach uses particle splitting and Russian roulette that consists in generating additional photons with a multiplicity value depending on the particle position, with the idea that the particles close to the detector have larger contributions than others. The speedup compared to analog simulation was estimated to be between 5 and 15. The angular response function (ARF) (Song *et al* 2005, Descourt *et al* 2010) is another acceleration method that computes detector response tables according to photon angles and energies (θ, ϕ, E). Tables only need to be computed once, and are used during simulations to reduce tracking time into the SPECT head. The forced detection (FD) method (De Beenhouwer *et al* 2008) directs a particle towards the detector for every interaction. The particle is weighted according to the probability that a particle with such direction would exist. The acceleration compared to an analog simulation was estimated between 105 and 159. Multiple projection sampling (MPS) (De Beenhouwer *et al* 2008, Liu *et al* 2008) uses FD on several detectors at the same time and is up to 60 times faster than a regular FD Monte Carlo. Convolution based forced detection (CFD) (Liu *et al* 2008) uses FD with a Gaussian blurring kernel to spread the signal onto the image. It was recently used with SIMIND (Karamat and Farncombe 2017) for an estimated six orders of magnitude gain over analog GATE simulations. The main differences between the published methods and the one proposed in this article are the detector responses (ARF versus convolution) and FD, which, in our case, is performed for all detector pixels and take into account phantom specific attenuation along all paths, not only the path perpendicular to the detector. Finally, fixed forced detection (FFD) was used for x-ray imaging (Colijn and Beekman 2004, Freud *et al* 2005, Poludniowski *et al* 2009). It uses FD onto a set of points (all detector pixels or a reduced number) then uses interpolation for the other pixels.

Multiple platforms are used to simulate PET/SPECT images (SimSET (Harrison *et al* 1993), SIMIND (Ljungberg and Strand 1989), Geant4/GATE (Jan *et al* 2011)). Simulation system for emission tomography (SimSET) is a specialized package optimized for PET/SPECT simulations. It uses a photon history generator to simulate photon interactions and transport inside a voxelized phantom. It contains several variance reduction techniques. GATE is widely used for SPECT simulations (Konik *et al* 2012, Spirou *et al* 2015), with modules available to perform photon tracking in a voxelized medium (generally obtained from a CT image), to manage a voxelized source of photons or any radionuclides, and to model the complete chain of the detector digitizer. It allows the generation of different energy windows and takes into account the energy resolution and the dead-time, as well as the intrinsic spatial resolution of the detector. It has been shown to be accurate compared to experimental measures (Assie *et al* 2010, Lee 2013). Several VRT techniques described before (FD, MPS, CFD) were developed for GATE (De Beenhouwer *et al* 2004, 2008). However, these were mostly proofs of concept and are not available in GATE with the exception of ARFs. Monte-Carlo SPECT simulation of real SPECT imaging devices remains a complex and long computing process and its acceleration is still required. The purpose of this article is to investigate FFD for SPECT simulation, which, to the best of our knowledge, has never been investigated for this modality.

2. Materials and methods

The proposed method uses fixed FD for accelerating SPECT simulations. In SPECT imaging, photons are emitted by radionuclides inside the patient or the phantom. A fraction of the photons that escape the patient reach the SPECT head. The collimator intercepts most of the photons that are not perpendicular to the detector plane. The remaining photons are detected by a pixelated detector. Some scattered photons can still reach the detector plane and blur the image. Because photons lose energy during Compton scattering, detectors can be energy sensitive to separate the incoming photons into several energy windows: the *primary window* (around the radionuclide peak(s)) and the *scatter window*. The scatter window may be used to reduce the noise in the primary windows with double or triple energy window scatter correction methods (Buvat *et al* 1994, Hutton *et al* 2011). In the following, we first describe the FFD technique, then the link with the ARF method. We investigate the production of a single projection view here. All developments were made within the GATE platform using Geant4 10.2 (Sarrut *et al* 2014).

2.1. Fixed forced detection

The FFD method was initially published in Colijn and Beekman (2004), Freud *et al* (2005) and Poludniowski *et al* (2009) for x-ray imaging. FFD is a variance reduction technique that forces photons towards each pixel of the detector for every Monte-Carlo interaction, which are of type $t \in \{\text{decay, Rayleigh scattering, Compton scattering, fluorescence}\}$. These photons are given a weight that depends on their probability to reach the SPECT head and can be separated into a *scattering* and a *transmission* probability. The scattering probability is the probability for the photon to be directed towards the pixel, according to the interaction type t of the photon. The transmission probability is the probability of the photon reaching the pixel according to the traversed medium (Beer–Lambert law). The final detector count value S_j for a pixel j is the product of these probabilities for each interaction $i \in I$. The probabilities are computed under the assumption that the attenuation and the differential cross section, which are computed at the center $\mathbf{p}_j$ of pixel j, are representative of all x-rays impinging the pixel surface. S_j is given by equation (1).

$$S_j = \sum_I \Delta\Omega_j(\mathbf{x_i}) \underbrace{\frac{1}{\sigma_{t_i}(E_i, Z_i)} \frac{\mathrm{d}\sigma_{t_i}}{\mathrm{d}\Omega}(E_i, Z_i, \theta_{ij})}_{\text{scattering}} \underbrace{a(E_{ij}, \mathbf{x}_i, \mathbf{p}_j)}_{\text{transmission}} \tag{1}$$

where $\mathbf{x_i}$ is the 3D position at interaction i, σ_t is the cross section of interaction type t, $\mathrm{d}\sigma_t/\mathrm{d}\Omega$ is the differential cross section that depends upon (1) the interaction type t, (2) the energy E_i of the photon before scattering, (3) the atomic number Z_i of the material that triggered scattering and (4) the scattering angle θ_{ij}. E_{ij} is the energy after scattering. a is the absorption from the interaction point to the pixel given by the the Beer–Lambert law equation (2) where $\mu(E, \boldsymbol{x})$ is the 3D distribution of the energy-dependent linear attenuation coefficients.

$$a(E, \mathbf{x}, \mathbf{p}) = \exp\left(-\int_0^1 \mu\left(E, \mathbf{x} + \alpha(\mathbf{p} - \mathbf{x})\right) \mathrm{d}\alpha\right) \tag{2}$$

$$\Delta\Omega_j(\mathbf{s}) \approx \Delta S \frac{(\mathbf{s} - \mathbf{p}_j) \cdot \mathbf{n}}{\|\mathbf{s} - \mathbf{p}_j\|^3}. \tag{3}$$

In equation (1), $\Delta\Omega_j(\mathbf{s})$ is the solid angle corresponding to pixel j observed from point $\mathbf{x}_i$ and $\mathbf{p}_j$ the 3D spatial position of the center of the pixel j. We consider that the distance between $\mathbf{x}_i$ and $\mathbf{p}_j$ is large enough to approximate the calculation of the solid angles using equation (3), with the pixel surface ΔS and $\mathbf{n}$ the unit detector nor-

mal to the detector and oriented towards the source **s**. Note that for a clinical SPECT, the distance is larger than a few centimeters while the pixel spacing is a few millimeters.

The distribution of linear attenuation coefficients $\mu(E, \mathbf{x})$ depends on the material definition, the physics list and the used cuts. It was computed with Geant4 using the `G4EmCalculator` class for every material of the voxelized phantom. The differential cross sections $\mathrm{d}\sigma_t/\mathrm{d}\Omega$ used in equation (1) were also retrieved from Geant4 using the `G4CrossSectionHandler` class. To implement equation (1), a ray-casting was performed from each interaction point towards all pixels of the detector. The ray-casting was discretized and performed using the reconstruction toolkit RTK (Rit *et al* 2014) with Joseph's algorithm (Joseph 1982). The ray-casting is independent for all pixels and was thus parallelized (multi-threaded CPU) for further computation gain. Note that all photons were forced with the FFD techniques, not only emitted primary photons but also all scattered ones, including multiple scattering.

2.2. Linking FFD with the ARF

The FFD method computes the probability for a photon to be directed towards a pixel and to reach it without further interaction. Two options were implemented to manage these photons upon reaching the detector. The first method passes photons outside of the volume back into the analog Monte-Carlo (AMC) simulation with their respective directions, energies and weights. They are then tracked by the Monte-Carlo engine. The second option links the output of the FFD directly to an ARF table (Descourt *et al* 2010). It eliminates the creation of thousands of photons and further reduces the computation time. In the following, we consider this second option.

The ARF method uses Monte-Carlo simulations to compute a tabulated response function of the SPECT detector. It computes the probability of detection for incident photons depending on their energy (E) and polar angles (θ, ϕ) with the detector plane. Every photon reaching the SPECT head is stopped and a detection probability is stored in the pixel in the trajectory of the photon. This function avoids photon tracking through the collimator and detector. Contrary to AMC where most photons will be absorbed in the collimator (only around 1 in 10^3 or 10^4 emitted photons will be detected for standard SPECT systems), every incident photon will deposit with the ARF some weighted count and contribute to the image formation (Descourt *et al* 2010).

Computing the tabulated functions is a lengthy process: about 10^9 to 10^{10} emitted primary photons are required to obtain a good statistical uncertainty for an energy window. For example, figure 1 shows the case of a $^{99\mathrm{m}}$Tc source. The photon energy spectrum has a main γ-ray emission at 140.5 keV (88.5% of decays). In this case, the digitizer is composed of two energy windows, the primary window [126.45,154.55] keV and the scatter window [114,126] keV, sampled with 6.6 keV steps, except for the 1 keV step of the 140.5 keV peak. Seven tables were computed for the $^{99\mathrm{m}}$Tc windows.

Once the tables are computed, they can be used for every simulation having the same conditions (same collimator/detector and radionuclide energy windows), independently of the source distribution and the medium, phantom or patient. ARF tables require little disk space, in this case, around 57 MB for seven tables. When using another radionuclide, such as ^{111}In, more tables are needed to keep the same energy resolution (six for the 171 keV peak, eight for the 245 keV peak and four for the scatter). In the following, we used the implementation proposed in GATE by Descourt *et al* (2010).

3. Experiments

The proposed method was compared to AMC simulations, used as reference. The quality of the simulated images was assessed using the projection images and quantified using the root mean square distance (RMSD) defined as:

$$\mathrm{RMSD} = \sqrt{\frac{\sum_{j=1}^{\mathrm{P}} \left(\bar{X}_j - \bar{X}_j^{\mathrm{ref}}\right)^2}{\mathrm{P}}} \tag{4}$$

with $\bar{X}_j$ the sample mean value at pixel j in the FFD image, $\bar{X}_j^{\mathrm{ref}}$ the sample mean pixel value in the reference image obtained by analog Monte Carlo, and P the number of pixels. The sample mean values were obtained by the batch method (Walters *et al* 2002). $N = 20$ batches were used for all experiments. We used the normalized RMSD (NRMSD) defined as: $\mathrm{RMSD}/X^{\mathrm{ref}}$, with $X^{\mathrm{ref}} = \sum_j X_j^{\mathrm{ref}}$. This criteria integrates both accuracy and precision and is limited by the relative statistical uncertainty s of the reference Monte Carlo. s is estimated by $s = \sigma/X^{\mathrm{ref}}$, with σ^2 the variance averaged over the image $\frac{1}{n}\sum_j \sigma^2(X_j^{\mathrm{ref}})$. If X_j in equation (4) were truly the unbiased mean, NRMSD would still be s. The variance $\sigma^2(X_j^{\mathrm{ref}})$ at pixel j was obtained using:

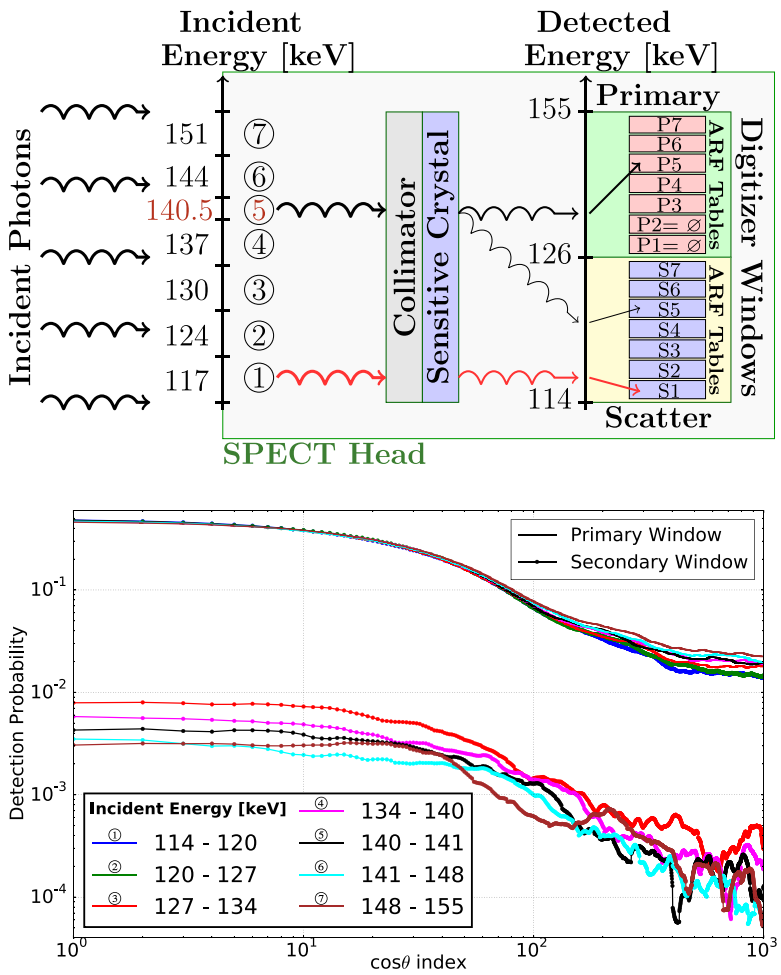

Figure 1. Top: schematic ARF table computation for a ^{99m}Tc source. The digitizer windows are divided into small energy ranges of 7 keV with smaller ones for the photo-peaks (indicated by ⑤ here). Two energy windows, primary and scatter, are shown, with the corresponding bins. Bottom: ARF tables for ^{99m}Tc with angle $\phi = 0$. There are five curves for the primary window (1 and 2 are below the range) and 7 for the secondary window. We used the notation of Descourt *et al* (2010): the cos θ index represents the binning of cos θ (from 0 to 1 with 2048 bins).

$$\sigma^2(X_j) = \frac{\sum_{b=1}^{N}(X_j^b - \bar{X}_j)^2}{N(N-1)} \tag{5}$$

where N is the number of batches, X_j^b is the value of X in batch b in pixel j, and $\bar{X}_j$ is the mean value of X in pixel j evaluated over all batches.

The computation time was assessed by computing the simulation efficiency ϵ_j in each pixel j:

$$\epsilon_j = \left[t \times \sigma^2(X_j)\right]^{-1} \tag{6}$$

where t is the total simulation time, $\sigma^2(X_j)$ the variance in pixel j. Hence, the efficiency is increased if the time taken to obtain a given variance on the quantity of interest is reduced. The gain G_j in a pixel j is defined as the efficiency ratio between the two methods m1 and m2: $G_j = \epsilon_j^{\mathrm{m1}}/\epsilon_j^{\mathrm{m2}}$.

3.1. First experiment: simple phantoms

The first test T_1 was the SPECT projection of an isotropic cubic source of 10 cm side of ^{99m}Tc inside a 20 cm cubic box. The box was either composed of air (T_{1a}) or water (T_{1b} and T_{1c}). As we are interested in voxelized volumes, we considered the box as a matrix of 100^3 voxels. The ^{99m}Tc source was modeled as a 140.5 keV gamma source. The simulated SPECT device was one head of a GE Discovery 670 with a NaI crystal (field of view of 54 cm $\times$ 40 cm) equipped with a parallel-hole collimator. The low-energy high-resolution collimator, with holes diameter of 1.5 mm and holes height of 35 mm, was modeled. In GATE, the *digitizer* module describes the global detector response and the signal processing chain after the gamma interactions in the crystal, replacing the PMTs that are not explicitly simulated (Jan *et al* 2011). We chose a spatial blurring of 5 mm, and the two energy windows

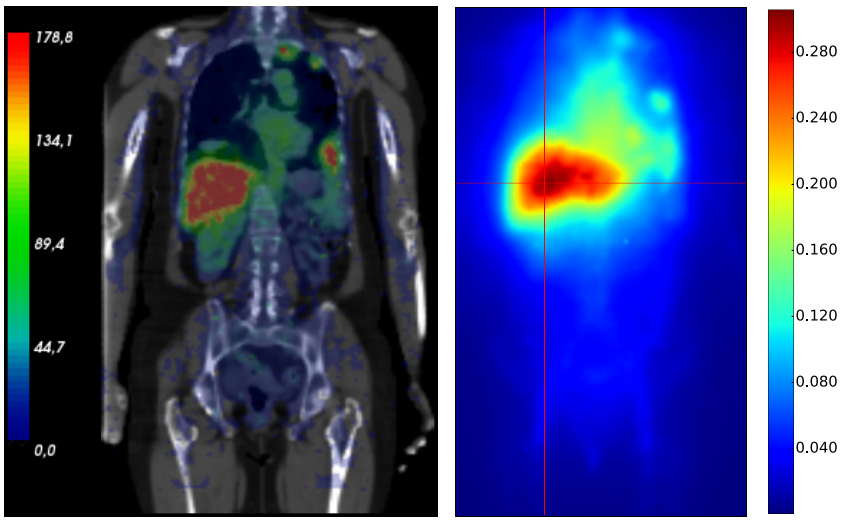

Figure 2. Left: activity map superimposed on a coronal slice of the CT scan; the scale indicates the number of counts in the voxels. Right: FFD + ARF projection image obtained with 7×10^6 emitted primaries; the scale indicates the number of detected counts in the pixels.

described above. The physics list used was `emstandard_opt3` with production cuts for gamma equal to 0.1 mm. The projections was defined with 100×100 pixels of 4 mm side.

3.2. Second experiment: clinical data

The second test T_2 was a complete SPECT simulation with both a CT image and a voxelized activity source obtained from real clinical data. The data were gathered from a clinical trial that studied a labeled monoclonal antibody (mAb), named ^{90}Y-OTSA101, targeting synovial sarcoma. In this trial, the dosimetry planning was performed from SPECT images acquired at several time point after ^{111}In-OTSA101 injection. We selected one patient and a time integrated activity map was computed and used as a voxelized activity source (Sarrut *et al* 2017). The CT of the patient, resampled to $2 \times 2 \times 2$ mm^3, was used in the simulation. The ^{99m}Tc voxelized source was $4 \times 4 \times 4$ mm^3. Figure 2 illustrates the input data.

4. Results

4.1. Test 1

The accuracy of the FFD method was evaluated using NRMSD versus both AMC and ARF. Figure 3 shows transverse profiles of simulated projection images for T_{1a} (in air, primary window), T_{1b} (in water, primary window), T_{1c} (in water, scatter window). The numbers of emitted primaries for AMC were 68×10^9 for T_{1a} and T_{1b}, and 165×10^9 for T_{1c}. With FFD method, the numbers of emitted primaries were around 1×10^6. Those numbers were chosen for practical reasons, leading to manageable computation times on the cluster. The use of equation (6) allowed us to compare them even if they did not lead to the same variance or detected counts.

The shape of the profiles were very similar, with an NRMSD below 3.5% between analog and FFD + ARF methods. The efficiency of each method was computed with a batch method (20 simulations each) for T_{1a}, T_{1b} and T_{1c}. The mean gains are given in table 1. Figure 4 shows the gains G pixel by pixel. The total detected counts in the simulated images with AMC were around 2, 4 and 8 million counts, respectively, for T_{1a}, T_{1b} and T_{1c}, which correspond to sensitivity of around 3×10^{-3}, 8×10^{-3} and 4×10^{-5}. The approximate computing speed was around 1300–2000 tracked particles per seconds (PPS) for the AMC method while around only 35–50 PPS for FFD method (Intel Xeon CPU E5-1660 3.30 GHz), obviously much slower due to the ray casting.

4.2. Test 2

For T_2, figure 5 shows the transverse and longitudinal profiles of the simulated projection image in figure 2 right. The numbers of emitted primaries were 4×10^{10} (analog), 10^{10} (ARF) and 2×10^6 (FFD + ARF). The total computation time was 389 d for the AMC, 87 d for the ARF and 13 h for the FFD + ARF. The computations were performed on a cluster and converted to a total time for a single core (Intel Xeon CPU E5-1660 3.30 GHz). The profiles follow similar shapes. For ten billion particles, the NRMSD on the central image region was 7.2%, which can be compared to the relative statistical uncertainty of 6.3% in the same region. We therefore did not observe any bias of FFD in comparison to the AMC within the statistical uncertainty. The gain by pixel ranges from 1.3

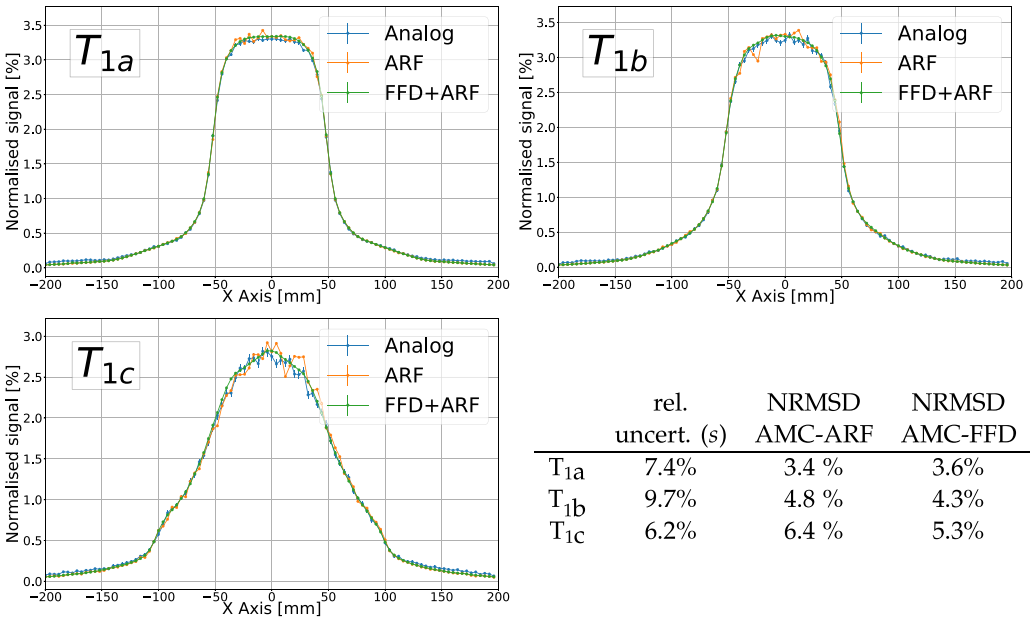

	rel. uncert. (s)	NRMSD AMC-ARF	NRMSD AMC-FFD
T_{1a}	7.4%	3.4 %	3.6%
T_{1b}	9.7%	4.8 %	4.3%
T_{1c}	6.2%	6.4 %	5.3%

Figure 3. Comparison of the analog, ARF and FFD + ARF profiles for the 10 cm cubic source in a 20 cm phantom (test 1). Left: phantom is composed of vacuum, primary window. Right: phantom is composed of water, primary window. Bottom: water phantom, scatter window. Relative statistical uncertainty of the reference Monte Carlo and NRMSD between AMC and ARF or FFD are summarized in the table.

Table 1. Mean gain over the whole image for analog, ARF and FFD + ARF. Phantom filled with vacuum (T_{1a}) or water (T_{1b},T_{1c}), on the primary (T_{1a},T_{1b}) or scatter window (T_{1c}).

Test	Analog versus ARF	ARF versus FFD + ARF	Analog versus FFD + ARF
T_{1a}	1.7×10^2	3.5×10^3	5.2×10^5
T_{1b}	4.2×10^2	1.5×10^3	2.1×10^5
T_{1c}	2.8×10^2	6.3×10^2	2.1×10^5

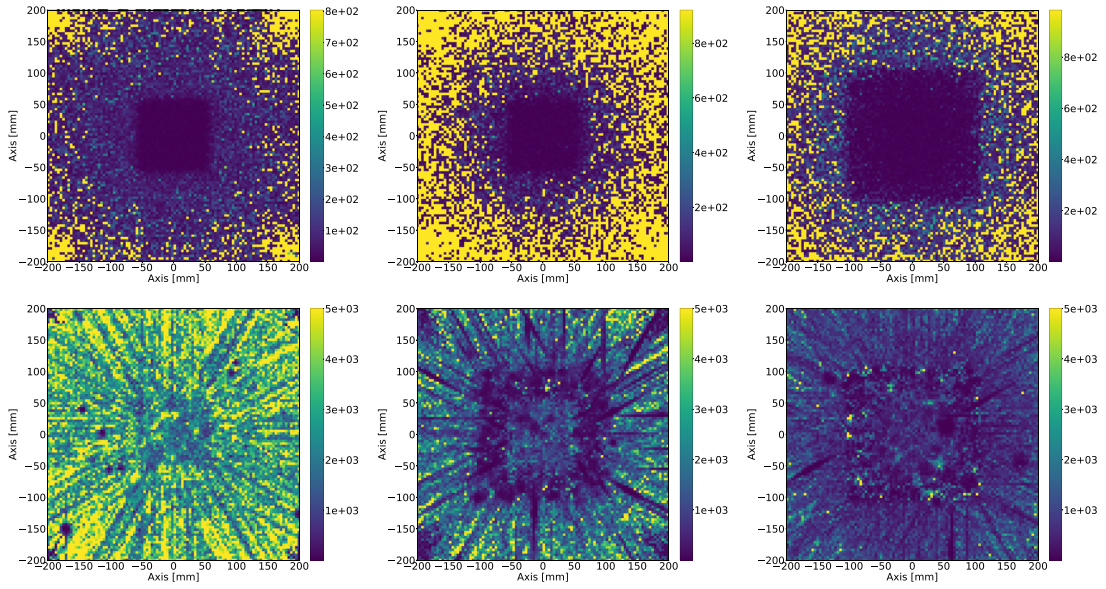

Figure 4. Gain map per pixel, the scales indicate the obtained acceleration factor G between the two compared methods. Top: comparison between ARF and analog. Bottom: comparison between FFD + ARF and ARF. Left: T_{1a}. Middle: T_{1b}. Right: T_{1c}.

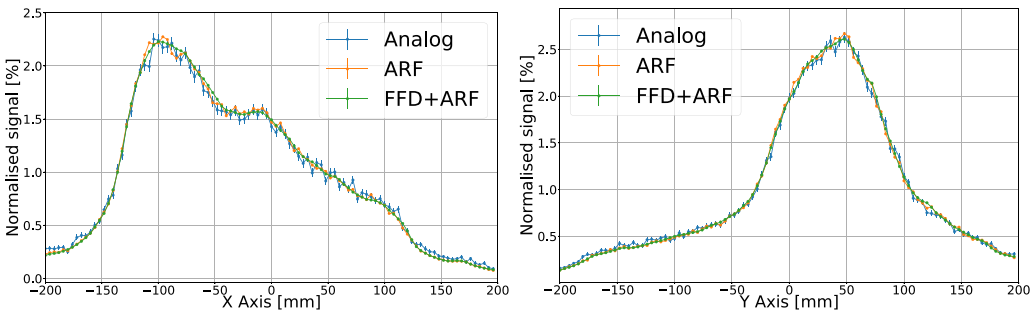

Figure 5. Transverse (left) and longitudinal (right) normalized profiles obtained on the simulated projected images of test 2 for the primary window. Profiles are shown for the AMC, ARF and FFD + ARF methods.

to 11×10^3 . The mean gain between the ARF versus FFD + ARF methods for pixels with more than 20% of the maximum signal was 760.

4.3. Convergence study

As already mentioned in previous works combining stochastic and deterministic strategies (Smekens *et al* 2009, 2014), 'hot spots' were observed when the statistic was not sufficient. Indeed, in a typical SPECT simulation, scattered particles are distributed in regions larger than the sources of emitting radionuclides. Therefore, the number of photons needed to get a representative sampling of the emitted particle's spatial distribution was larger for scatter than for primary photons. Because FFD allows for fast convergence of rare events, it can lead to bright spots before convergence. To clarify this phenomenon, simulations of a 10 cm edge size cubic source in a 20 cm cubic water phantom for different numbers of emitted primaries were computed. Resulting images were compared with the reference image obtained with 10^7 emitted primaries. In order to illustrate the role of (i) the primaries, (ii) the source size relatively to the phantom and (iii) secondary photons, we performed the simulations with varying source sizes (0.4, 2, 4, 10, 15 and 20 cm) and observed the differences in convergence speeds.

Figure 6 shows projection and RMSD images obtained with FFD + ARF for 10^2, 10^4 and 10^6 particles. Several 'hot spots' can be observed due to the spatial distribution of emitted primaries. In the last image, we can see brighter spots inside the source with a smaller RMSD (0.04) than for the second image (0.225).

Figures 7 (primaries only) and 8 (primaries and scattered photons) show precision and NRMSD according to the number of primaries (10^3–10^6): precision (right image) was quantified by the percentage of pixels with a relative statistical uncertainty below 2%. We choose 2% arbitrarily because this value this is a commonly chosen value in Monte Carlo papers, but other thresholds of interest may be used.

For primary photons, both the pixel convergence and the NRMSD decreases were correlated with the size of the source. For a 4 mm source, only 10^3 emitted primaries were needed to get less than 2% NRMSD and >95% pixel convergence, while 10^5 were required to obtain similar results with a source as large as the phantom (20 cm). When taking scattered photons into account, voxels that are far from the source will have a low photon count, thus larger sources meant a quicker convergence.

5. Discussion

The FFD method reached very good agreement with analog simulations for simple cases (T_{1a}, T_{1b}, T_{1c}) as well as for realistic cases (T_2 patient data). NRMSD values were always of the order of the relative statistical uncertainty, which indicated that the bias was much smaller than the Monte-Carlo uncertainty. Regarding efficiency, the gains were up to 10^3 compared to ARF only and 10^5 compared to analog. Also, as already pointed out by Song *et al* original ARF paper (Song *et al* 2005), the detection probability of gamma with incident angle larger than 15–20 degrees is close to zero (excepted for high energy gamma). Thus, additional time gain could be reached if gamma with a large incident angle is ignored during the FFD step. With other types of collimators, for example for high-energy radionuclide-like ^{131}I, efficiency may change slightly, but it has not been investigated here. Both the NRMSD and the statistical uncertainty were dependent on the size of the source. For a 2 cm source, only 3×10^3 emitted primaries were needed to obtain more than 95% of the pixels below 2% uncertainty and less than 2% NRMSD error, while 5×10^4 emitted primaries were needed when the source was larger (20 cm). A point source needs only one emitted primary to generate the projection image of detected primaries. When scattered photons are considered, the results were reversed: for a 20 cm source, 10^5 emitted primaries are needed to reach a NRMSD below 2% for 95% of the pixels, while 10^6 were needed for a smaller 2 cm source. In total, scattered photons represent in the water phantom 26% (23.8% Compton, 2.5% Rayleigh) of the total signal. Also, note

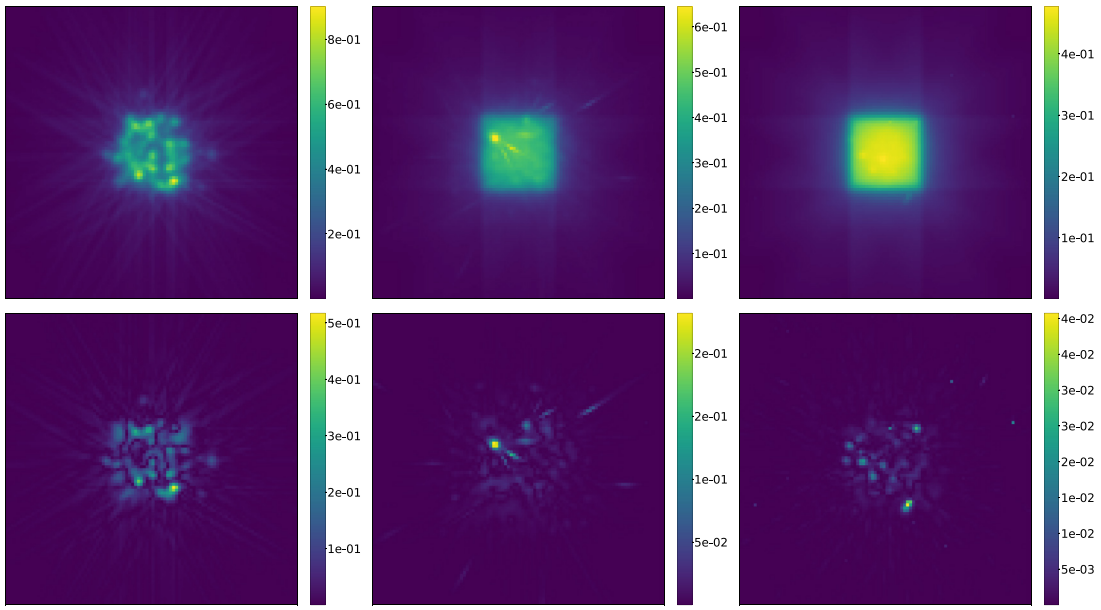

Figure 6. The top figures show SPECT projection images of a cubic source (10 cm) in a water phantom (20 cm) for different numbers of emitted primaries (10^2, 10^4, 10^6). The bottom figures show NRMSD between AMC and FFD in the same conditions.

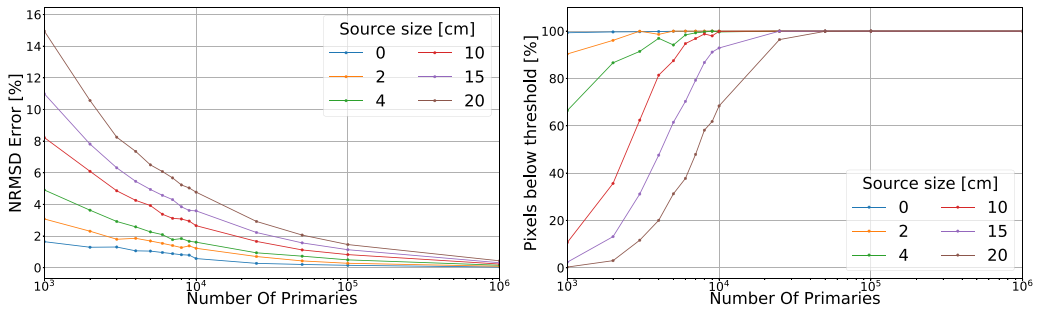

Figure 7. Evolution of the NRMSD (left) and percentage of pixels with a relative uncertainty below 2% (right) according to the number of emitted primaries (10^3–10^6), for primary photons only (not scatter).

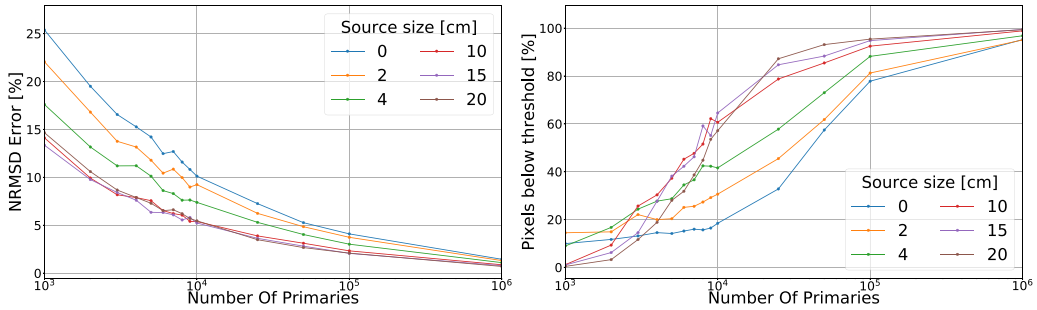

Figure 8. Evolution of the NRMSD (left) and percentage of pixels with a relative uncertainty below 2% (right) according to the number of emitted primaries (10^3–10^6), for both primary and scattered photons.

that, because of the proposed variance reduction, the obtained image will not contain a noise similar to the AMC method. If the user wants to reproduce it, the data should be scaled to the correct number of counts and be corrupted with Poisson noise.

Finally, we did not investigate a practical criterion to determine convergence because it mostly depends of the application and will be very different if the user is interested in detecting the primary signal or the scattered one in a particular region of the image. In the proposed implementation, only one voxelized volume can be used in a simulation and no other volumes could be positioned between this volume and the ARF plane.

6. Conclusion

We proposed a method to reduce the variance of Monte-Carlo SPECT simulations using FFD in order to get a better computation time. This implementation was further improved by linking the FFD to ARF tables. The measured gain versus analog simulations was up to five orders of magnitude for realistic patient simulations. For a relative statistical uncertainty below 2%, this method can simulate a projection in less than 2 h on a single core instead of days. Only a few simulations cases have been tested, further studies are needed for further adoption. This method with examples and documentation is available in the last GATE V8.0 version.

Acknowledgments

This work was partly supported by t-Gate ANR-14-CE23-0008, the SIRIC LYric Grant INCa-DGOS-4664 and the LABEX PRIMES (ANR-11-LABX-0063/ ANR-11-IDEX-0007).

ORCID iDs

D Sarrut https://orcid.org/0000-0002-4854-4141

References

Assie K, Dieudonne A, Gardin I, Vera P and Buvat I 2010 A preliminary study of quantitative protocols in Indium 1 1 1 SPECT using computational simulations and phantoms *IEEE Trans. Nucl. Sci.* **57** 1096–104
Buvat I, Benali H, Todd-Pokropek A and Di Paola R 1994 Scatter correction in scintigraphy: the state of the art *Eur. J. Nucl. Med.* **21** 675–94
Colijn A and Beekman F 2004 Accelerated simulation of cone beam x-ray scatter projections *IEEE Trans. Med. Imaging* **23** 584–90
De Beenhouwer J 2009 Acceleration of GATE Monte Carlo simulations *PhD Thesis* Gent University
De Beenhouwer J, Staelens S, Dressel M, D'Asseler Y, Vandenberghe S, Lemahieu I and Van de Walle R 2004 Geometrical importance sampling, pulse height tallies in gate *26th Annual Int. Conf. of the IEEE Engineering in Medicine and Biology Society* vol 1 (IEEE)
De Beenhouwer J, Staelens S, Vandenberghe S and Lemahieu I 2008 Acceleration of GATE SPECT simulations *Med. Phys.* **35** 1476–85
Descourt P, Carlier T, Du Y, Song X, Buvat I, Frey E C, Bardiès M, Tsui B M W and Visvikis D 2010 Implementation of angular response function modeling in SPECT simulations with GATE *Phys. Med. Biol.* **55** N253
Freud N, Létang J M and Babot D 2005 A hybrid approach to simulate multiple photon scattering in x-ray imaging *Nucl. Instrum. Methods Phys. Res.* B **227** 551–8
Harrison R L, Vannoy S D, Haynor D R, Gillispie S B, Kaplan M S and Lewellen T K 1993 Preliminary experience with the photon history generator module of a public-domain simulation system for emission tomography *IEEE Conf. Record Nuclear Science Symp. and Medical Imaging Conf.*
Haynor D R, Harrison R L and Lewellen T K 1991 The use of importance sampling techniques to improve the efficiency of photon tracking in emission tomography simulations *Med. Phys.* **18** 990–1001
Hutton B F, Buvat I and Beekman F J 2011 Review and current status of spect scatter correction *Phys. Med. Biol.* **56** R85
Jan S *et al* 2011 GATE V6: a major enhancement of the GATE simulation platform enabling modelling of CT and radiotherapy *Phys. Med. Biol.* **56** 881
Joseph P M 1982 An improved algorithm for reprojecting rays through pixel images *IEEE Trans. Med. Imaging* **1** 192–6
Karamat M I and Farncombe T H 2017 A comparison between gate and accelerated convolution-based forced detection simind for low- and medium-energy collimators: a simulation study *IEEE Trans. Radiat. Plasma Med. Sci.* **1** 36–45
Konik A, Madsen M T and Sunderland J J 2012 GATE simulations of small animal SPECT for determination of scatter fraction as a function of object size *IEEE Trans. Nucl. Sci.* **59** 1887–91
Lee S, Gregor J and Osborne D 2013 Development and validation of a complete GATE model of the Siemens Inveon trimodal imaging platform *Mol. Imaging* (https://doi.org/10.2310/7290.2013.00058)
Liu S, King M A, Brill A B, Stabin M G and Farncombe T H 2008 Accelerated SPECT Monte Carlo simulation using multiple projection sampling and convolution-based forced detection *IEEE Trans. Nucl. Sci.* **55** 560–7
Ljungberg M and Strand S E 1989 A Monte Carlo program for the simulation of scintillation camera characteristics *Comput. Methods Programs Biomed.* **29** 257–72
Poludniowski G, Evans P M, Hansen V N and Webb S 2009 An efficient Monte Carlo-based algorithm for scatter correction in keV cone-beam CT *Phys. Med. Biol.* **54** 3847
Rit S, Vila Oliva M, Brousmiche S, Labarbe R, Sarrut D and Sharp G C 2014 The reconstruction toolkit (RTK), an open-source cone-beam CT reconstruction toolkit based on the Insight toolkit (ITK) *J. Phys.: Conf. Ser.* **489** 012079
Sarrut D, Badel J, Halty A, Garin G, Perol D, Cassier P, Blay J, Kryza D and Giraudet A 2017 3D absorbed dose distribution estimated by Monte Carlo simulation in radionuclide therapy with a monoclonal antibody targeting synovial sarcoma *EJNMMI Phys.* **4** 6
Sarrut D *et al* 2014 A review of the use and potential of the gate Monte Carlo simulation code for radiation therapy and dosimetry applications *Med. Phys.* **41** 064301
Smekens F, Freud N, Létang J M, Adam J F, Ferrero C, Elleaume H, Bravin A, Estève F and Babot D 2009 Simulation of dose deposition in stereotactic synchrotron radiation therapy: a fast approach combining Monte Carlo and deterministic algorithms *Phys. Med. Biol.* **54** 4671–85
Smekens F, Létang J M, Noblet C, Chiavassa S, Delpon G, Freud N, Rit S and Sarrut D 2014 Split exponential track length estimator for monte-carlo simulations of small-animal radiation therapy *Phys. Med. Biol.* **59** 7703
Song X, Segars W P, Du Y, Tsui B M W and Frey E C 2005 Fast modelling of the collimator-detector response in monte carlo simulation of spect imaging using the angular response function *Phys. Med. Biol.* **50** 1791–804
Spirou S V, Papadimitroulas P, Liakou P, Georgoulias P and Loudos G 2015 Investigation of attenuation correction in SPECT using textural features, Monte Carlo simulations, and computational anthropomorphic models *Nucl. Med. Commun.* **36** 952–61
Walters B R B, Kawrakow I and Rogers D W O 2002 History by history statistical estimators in the BEAM code system *Med. Phys.* **29** 2745–52